Surface & Coatings Technology 483 (2024) 130800



Contents lists available at ScienceDirect

Surface & Coatings Technology

journal homepage: www.elsevier.com/locate/surfcoat



Full Length Article



Mechanisms of permeation of helium, hydrogen, oxygen, and water vapor through silicate-based composite barrier coating layers

Stefan Schiessl [a,b,*], Esra Kucukpinar [b], René Schwiddessen [c], Horst-Christian Langowski [a,b], Peter Eisner [a,b]

[a] TUM School of Life Sciences, Technical University of Munich, Alte Akademie 8, 85354 Freising, Germany
[b] Department Material Science, Fraunhofer Institute for Process Engineering and Packaging, Giggenhauser Str. 35, 85354 Freising, Germany
[c] Department of Structure and Dynamics of Energy Materials, Helmholtz-Zentrum Berlin für Materialien und Energie GmbH, Hahn-Meitner-Platz 1, 14109 Berlin, Germany

ARTICLE INFO

Keywords:
Hydrogen permeation
Helium permeation
Oxygen permeation
Barrier composite
Montmorillonite

ABSTRACT

When considering coating of flexible films for the packaging of sensitive products, a common goal is to meet all gas barrier requirements in a single process step. One way to achieve this is to improve the barrier performance of polymeric coating layers by incorporating silicate particles. In order to tailor the gas barrier performance of the coatings, understanding the permeation mechanisms through these composite coating layers is required. In this study, polyethylene terephthalate films were coated with composite lacquers comprising montmorillonite particles and a polymer matrix. The compatibility of montmorillonite with polymer matrices of polypropylene, polyacrylate, polycarboxylic acid, and polyvinyl alcohol was tested. The permeation behavior of helium, hydrogen, oxygen, and water vapor in these coatings was investigated. For a composite coating layer comprising montmorillonite and polyvinyl alcohol at a mixing ratio of 1:1 by weight, barrier improvement factors of 49, 41, and 26 compared with the pure polymer coating were found for helium, hydrogen, and oxygen, respectively. It was shown that the permeability coefficients of composite coating layers decrease with increasing permeant kinetic diameter. A comparison of calculated and measured permeability values indicated that the integration of montmorillonite leads to a tortuous permeation path and changes in the free volume and crystallinity of the polymer matrix. The permeation mechanism for water vapor turned out to be completely different from that for non-polar helium, hydrogen, and oxygen and is determined by the so-called polar path effect.

1. Introduction

Gas permeation is an important topic in several application fields. Packaging materials for foods, cosmetics, healthcare products, and pharmaceutical products are considered to provide specific gas barriers against oxygen, water vapor, and volatile compounds [1]. Organic solar cells and flexible organic field-effect transistors need to be encapsulated with high barrier films against oxygen and water vapor to ensure long-life stability, since the sensitive organic materials degrade in the presence of water or oxygen molecules [2,3]. Hydrogen storage and the associated barrier against hydrogen in mobility or energy storage applications are a long standing topic [4]. Furthermore, newly developed bioelectronic implantable systems need to be protected from harsh environment consisting of biofluids, water-based solutions, and different ions [5]. The helium barrier is rarely a direct requirement, such as when sealing hard drives, as their housings are filled with helium and sealed to reduce friction at high revolution speeds [6]. However, the helium barrier is often determined since this measurement is a rapid, reliable, and commonly used method to characterize the barrier properties of materials [7,8].

There are several technologies for creating a gas barrier on flexible films. These include vacuum processes, i.e. physical and chemical vapor deposition, and atmospheric pressure wet coating processes, i.e. coating with barrier lacquers [9,10]. Even higher gas barriers are reached by combining the aforementioned processes or by increasing the number of coating layers to a layer-by-layer (LbL) assembly [11–14]. An option

* Corresponding author at: Department Material Development, Fraunhofer Institute for Process Engineering and Packaging, Giggenhauser Str. 35, 85354 Freising, Germany.
E-mail address: stefan.schiessl@ivv.fraunhofer.de (S. Schiessl).

https://doi.org/10.1016/j.surfcoat.2024.130800
Received 19 February 2024; Received in revised form 2 April 2024; Accepted 14 April 2024
Available online 18 April 2024
0257-8972/© 2024 The Author(s). Published by Elsevier B.V. This is an open access article under the CC BY license (http://creativecommons.org/licenses/by/4.0/).

that allows keeping the number of process steps low is to improve barrier coating layers by the integration of impermeable platelet-shaped particles, e.g. montmorillonite (MMT) [15–18].

Such a barrier coating is, for example, polyvinyl alcohol (PVA), which is known for its compatibility with MMT. In a previous study, the authors achieved, for example an oxygen barrier improvement factor of 12 and a helium barrier improvement factor of 17 when 50 wt% MMT with respect to the dry mass was incorporated in PVA coating layers [19]. The improvement factor (see Eq. (11) later) describes the change in permeability of a pure polymer layer on addition of impermeable particles. The addition of MMT to polypropylene (PP) is commonly performed in a melt-mixing step, which limits the amount of MMT to be mixed with PP [20]. Sirousazar et al. [21] found, for example, barrier improvement factors of 1.7 and 2.5 for oxygen and water vapor, respectively, when 10 wt% MMT was added to the PP melt. The barrier of polymer-silicate composites against hydrogen has attracted increasing interest. Conde-Wolter et al. [22] measured, for example, a hydrogen barrier improvement factor of 3.0 from 7.6×10^2 to 2.6×10^2 $\frac{cm^3\,(STP)}{m^2\,d\,bar}$, when 48 wt% carbon fibers were integrated in polycaprolactam thermoplasts and a hydrogen barrier improvement factor of 3.7 from 9.6×10^2 to 2.6×10^2 $\frac{cm^3\,(STP)}{m^2\,d\,bar}$ when 55 wt% carbon fibers are incorporated in polyphthalamide thermoplasts.

In this work, the gas barrier properties and mechanisms of permeation of helium, hydrogen, oxygen, and water vapor through composite coating layers were investigated. When investigating gas permeation through composite barrier layers, it is particularly important to examine the polarity of the permeant and lacquer, the effect of filler content, the interaction between polymer and filler, the effect of the layer thickness, and temperature and humidity at which the measurements are performed. The polymer materials were a PP dispersion, a polyacrylic dispersion (PAD), a polycarboxylic solution (PCS), and a PVA solution in the form of aqueous lacquers. Thus, two dispersions and two solutions varying in polarity were selected. These lacquers were mixed with an MMT dispersion in such a way that composite lacquers with two mixing ratios of polymer:MMT of 3:1 and 1:1 were produced. MMT was selected because of its compatibility to PVA is known to the authors [19,23]. Moreover, MMT is market-available, naturally abundant, and does not disturb recycling processes.

The surface energies of the polymer lacquers and the MMT dispersion were measured in liquid (pendant drop) and dried (sessile drop) states. The comparison of these values provides information on influences on the hydration shell of the MMT particles in the composite mixture. Viscosity measurements were performed for the pure lacquer systems and the mixed composites and the shear-thinning behaviors were compared, indicating interactions between the polymer matrix and the MMT. Fourier-transform infrared (FTIR) spectra were measured for all coating layers, and peak shifts from pure systems to composites were investigated to reveal interactions in the dried state. X-ray measurements of the coating layers were performed to determine the influence of the addition of MMT on the polymer matrix's crystallinity. Pole figures generated from the XRD data were used to evaluate the orientation of the MMT platelets in the coating layers. The barrier improvement due to MMT particles was determined for gases varying in gas kinetic diameter and polarity, i.e. helium, hydrogen, and oxygen, and polar water vapor. Since helium and the other noble gases are the only gases that permeate through polymers at moderate temperatures in atomic form, helium possesses the smallest gas kinetic diameter of 2.60 Å. Hydrogen and oxygen permeate in molecular form and have gas kinetic diameters of 2.89 and 3.46 Å, respectively. The polar water molecule has a gas kinetic diameter of 2.65 Å [24]. For hydrogen and oxygen, the barrier performance was measured at different temperatures, to calculate the activation energy for permeation via the Arrhenius approach. In addition to the measured values, the potential barrier improvement due to MMT particles was calculated according to the tortuous path theory developed by Nielsen [25]. The comparison of measured and calculated values of the permeability coefficients indicates the main influencing factors for the permeation of the respective gases through the composite coating layers.

2. Materials and methods

2.1. Materials

Four different polymer matrix materials, in the form of aqueous lacquers, were used. The first lacquer was a polypropylene dispersion (PP), Aquaseal X2257 from Paramelt (Heerhugowaard, The Netherlands), with a particle size of less than 0.7 µm. It is a milky white liquid stabilized at an alkaline pH value of 10. The second lacquer was a polyacrylic dispersion (PAD), Loctite Liofol HS 59-605 RE from Henkel (Düsseldorf, Germany), with a particle size of less than 0.3 µm. The milky white aqueous dispersion contains a solid content of 44 % and has a slightly alkaline pH value of 8 to 9. The third lacquer was an aqueous solution of modified polycarboxylic acid and a small amount of polyethylenimine (PCS), Epotal BLX 3680 X from BASF (Ludwigshafen am Rhein, Germany). The solution contains 18 wt% solid content, is slightly yellowish, and has a pH value between 8 and 10. The fourth lacquer, Exceval AQ-4104 from Kuraray (Frankfurt, Germany), is mixed from polyvinyl alcohol (PVA) granulate and demineralized water to a targeted solid content. For this study, a solid content of 15 wt% was prepared according to the previously described procedure [19]. It is a transparent solution with a slightly acidic pH value of 5 to 7. Platelet-shaped MMT particles, CLOISITE Na^+, were purchased from BYK Additives and Instruments (Wesel, Germany). Polyethylene terephthalate (PET), HOSTAPHAN®RN23, from Mitsubishi Polyester Film (Wiesbaden, Germany) was used as a transparent substrate film with a thickness of 23 µm. Polytetrafluoroethylene (PTFE) film, used to characterize the dispersive and polar parts of the lacquers' surface energy, had a thickness of 100 µm and was obtained from RCT Reichelt Chemietechnik (Heidelberg, Germany).

2.2. Sample preparation

2.2.1. Lacquer formulation

All composite lacquers were produced in a similar way. The MMT dispersion was prepared with a planetary ball mill as described by Schiessl et al. [19] with a solid content of 5 wt%. Table 1 lists the amounts of polymer lacquer, MMT dispersion, and demineralized water used to mix the lacquers. First, the MMT dispersion was weighed in a beaker together with the demineralized water and homogenized with a magnetic stirrer. Subsequently, the respective amount of polymer lacquer was added via a pipette slowly under constant stirring. The beaker was closed and the composite lacquer was stirred for 10 min. For each polymer matrix, the (diluted) polymer lacquer without MMT particles as reference (ref) and the two composite lacquers with a mixing ratio of 3:1 and 1:1 by weight of polymer solid and MMT solid were prepared. The parameters that were kept constant for all coatings were the mixing ratios and the targeted dry layer thickness of 1 to 3 µm. Some polymer lacquers had to be diluted slightly to reach the required dry layer thickness with the k-bars.

2.2.2. Sheet coating

Before coating, the PET sheets of DIN A4 size were physically pretreated via corona discharge with a dose of 2.9 $\frac{kJ}{m^2}$ applied with a table corona unit from Tigres (Marschacht, Germany) to reach a minimum surface energy of 44 $\frac{mN}{m}$. The prepared lacquers were coated on the sheets with a lab-coating unit, type CUF 5 (Sumet Messtechnik, Denklingen, Germany), using the k-bar technique. The drying was performed for 2.5 min at 90 °C. Since the total solid content of each lacquer was different, k-bars providing different wet layer thicknesses were used to end up with a dry coating thickness between 1 and 3 µm (Fig. S4-S15).

Table 1
Lacquer composition with shares of polymer lacquer, MMT dispersion, and demineralized water leading to respective total solid contents.

sample	mass (polymer lacquer) g	m (MMT dispersion) g	m (water) g	total solid content %
PP-ref	55.6	0.00	94.4	20
PP(3):MMT(1)	20.8	75.0	54.2	10
PP(1):MMT(1)	6.94	75.0	68.1	5.0
PAD-ref	68.2	0.00	81.8	20
PAD(3):MMT(1)	25.6	75.0	49.4	10
PAD(1):MMT(1)	8.52	75.0	66.5	5.0
PCS-ref	83.3	0.00	66.7	10
PCS(3):MMT(1)	31.2	37.5	81.3	5.0
PCS(1):MMT(1)	10.4	37.5	102	2.5
PVA-ref	150	0.00	0.00	15
PVA(3):MMT(1)	37.5	37.5	75.0	10
PVA(1):MMT(1)	25.0	75.0	50.0	5.0

The pure MMT dispersion was coated with an initial solid content of 5 wt% on similarly prepared PET to produce a reference layer (MMT-ref) without polymeric binder.

2.3. Methods

2.3.1. Determination of surface energies of liquid and dried lacquers

The total surface energy of the lacquers γ_l was measured according to DIN EN ISO 19403-3 [26] via the pendant drop method at 23 °C. A requirement for this method is to know the density of the test liquid. Therefore, the density was measured for each liquid using a DSA 100 hydrometer from Kruess (Hamburg, Germany).

The lacquers were placed with a drop volume of 10 to 15 µL on a nearly pure dispersive solid, PTFE, according to the sessile drop method. The contact angle between the lacquers and the PTFE surface was denoted α. The surface energy γ_s of PTFE is 15.2 $\frac{\text{mN}}{\text{m}}$, distributed as a dispersive component of 14.8 $\frac{\text{mN}}{\text{m}}$ and a polar component of 0.4 $\frac{\text{mN}}{\text{m}}$. The dispersive γ_l^d and polar γ_l^p components of the lacquers were calculated according to Eq. (1) and Eq. (2) [27].

$$\gamma_l^d = \frac{\gamma_l \gamma_s (1 + cos(\alpha))}{4\gamma_s - \gamma_l (1 + cos(\alpha))} \quad (1)$$

$$\gamma_l^p = \gamma_l - \gamma_l^d \quad (2)$$

The surface energies of the dried lacquer and of the pure MMT layer were measured according to DIN EN ISO 19403-2 [28] via the sessile drop method. For this purpose, at least five drops of three different liquids, water, ethylene glycol, and diiodomethane, were placed with a drop volume of 3 µL on the surface, and the contact angle was measured at equilibrium.

2.3.2. Fourier transform infrared (FTIR) spectroscopy

The FTIR spectra were measured with a Frontier™FTIR spectrometer L1280034 from PerkinElmer (Shelton, CT, USA) in the ATR (attenuated total reflectance) mode with a diamond crystal. All spectra were baseline corrected. PerkinElmer Spectrum IV Version 10.6.1 software was used to analyze the spectra. A total of 32 scans with a resolution of 2 $\frac{1}{\text{cm}}$ were recorded within a wavenumber range from 4000 to 600 $\frac{1}{\text{cm}}$.

2.3.3. Determination of the viscosity of the lacquer formulations

Rheological measurements were performed in a cone-plate set-up with a 50 mm diameter cone, an angle of 0.995°, and a gap size of 100 µm. The rheometer used was a modular compact rheometer 302 from Anton Paar (Graz, Austria). For each lacquer, a shear sweep measurement was performed from 3 to 3000 $\frac{1}{\text{s}}$ at room temperature (23 °C) with a logarithmically increasing step size limited to 46 measuring points. Threefold measurements were performed for all lacquers and average values with standard deviations are shown in the Figures.

2.3.4. Determination of X-ray diffraction pattern and pole figures

X-ray diffraction (XRD) data were collected with a PANalytical X'Pert Pro MDP X-ray diffractometer (Almelo, The Netherlands) using Cu-K_α radiation (λ = 1.541 84 Å) equipped with an Xe proportional counter in grazing incidence geometry (angle of incidence: 2°).

The pole figures were obtained using a PANalytical X'Pert Pro MRD X-ray diffractometer (Almelo, The Netherlands) equipped with a Eulerian cradle employing two-axis scans along ϕ (rotation) and χ (tilt). Measurements were performed at a fixed 2θ angle of 6°, corresponding to the 2θ angle position of the (001) lattice plane of MMT. To plot pole figures, the intensity distribution was measured along the sample rotation angle ϕ from 0 to 360° at sample tilts χ from −85 to 85° with an increment of 5° each. After averaging the intensity for each rotation angle, the intensity was plotted against the sample tilt χ. From this graph a numerical value describing the orientation degree of the platelet-shaped particles in the coating layer can be calculated as the integral breadth. This value is defined as the ratio of the peak area and the peak height. Taking the integral from 0 to 85° gives the average alignment angle ζ between the MMT platelets and the substrate surface. The alignment angle describes the orientation of the platelets in the coating layer.

2.3.5. Helium permeability coefficients

The helium permeance Q_{He} was measured with a QHV-4 permeameter (Vinci Technologies, Nanterre, France) using a patented protocol [29]. In this measurement device, a mass spectrometer detects an ion current proportional to the permeation rate of the gas. Duplicate determinations were performed at 23 °C and 0 %RH. First, a helium calibrated leak was measured, then the baseline, and finally the helium permeance of the samples. The measurement was completed as soon as the measured permeation rate stayed constant for at least 2 h. For reliable comparability, the helium permeability coefficient P_{meas} of the coating layers was separately calculated for each sample. Therefore, the permeance of the coating layer $Q_{\text{He}}^{\text{coating}}$ was calculated from the measured total permeance of the coated film $Q_{\text{He}}^{\text{total}}$ and the known permeance of the uncoated film $Q_{\text{He}}^{\text{film}}$ (1.3×10^3 $\frac{\text{cm}^3\,(\text{STP})}{\text{m}^2\,\text{d}\,\text{bar}}$) via Eq. (3).

$$Q_{\text{He}}^{\text{coating}} = \frac{Q_{\text{He}}^{\text{film}} \cdot Q_{\text{He}}^{\text{total}}}{Q_{\text{He}}^{\text{film}} - Q_{\text{He}}^{\text{total}}} \quad (3)$$

Then, the helium permeability coefficient P_{meas} of the coated layer was calculated from the permeance $Q_{\text{He}}^{\text{coating}}$ via multiplication with the layer thickness, here in µm. In this case, the unit for P_{meas} was $\frac{\text{cm}^3\,(\text{STP})\,1\,\mu\text{m}}{\text{m}^2\,\text{d}\,\text{bar}}$ [30].

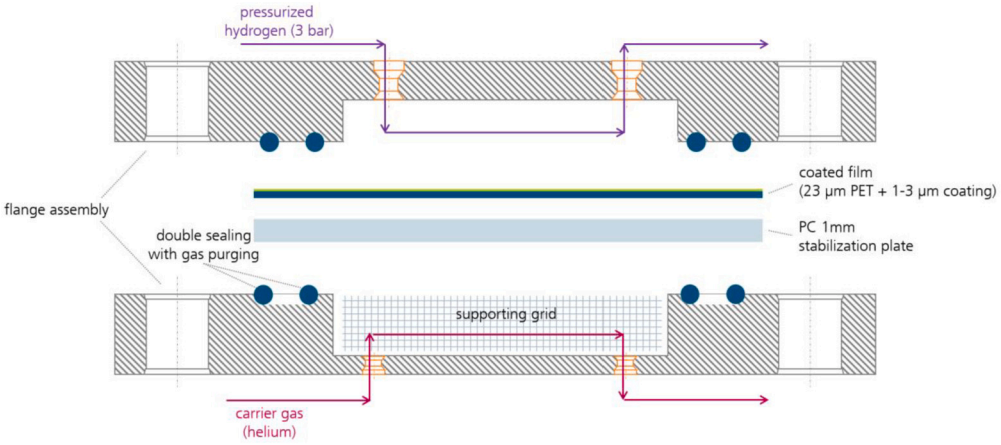


Fig. 1. 2D exploded-view drawing of the measuring cell used to measure hydrogen permeance.

2.3.6. Hydrogen permeability coefficients

The hydrogen permeance Q_{H_2} was measured with the measuring cell shown in Fig. 1. The measurement arrangement between the two cell parts comprised a 1 mm polycarbonate (PC) plate, which was placed on a double sealing ring. On top of the PC plate, a coated PET film was placed. The measuring area, which is the area covered by the inner sealing ring, was 54.45 cm^2. The second part with two sealing rings was fixed with a flange assembly to the first part. In the next step, pressurized hydrogen was conducted to the upper part of the measuring cell. Double sealing with helium gas purging in-between prevented side permeation. Since a total pressure difference of 3 bar was applied between the two chambers, the coated 23 µm thick PET film had to be supported by a 1 mm thick plate made of PC, a stable, but highly hydrogen-permeable material. A supporting grid was also used to prevent deformation of the PC plate. The permeating hydrogen was transported by the helium carrier gas to a mass spectrometer where it was detected. Again, twofold measurements were performed. As the hydrogen permeance of the PC plate $Q_{H_2}^{plate}$ (7.1×10^2 $\frac{cm^3\,(STP)}{m^2\,d\,bar}$) and the PET film $Q_{H_2}^{film}$ (1.8×10^3 $\frac{cm^3\,(STP)}{m^2\,d\,bar}$) are known, the hydrogen permeance of the coating layer can be calculated according to Eq. (4).

$$Q_{H_2}^{coating} = \frac{Q_{H_2}^{film} \cdot Q_{H_2}^{plate} \cdot Q_{H_2}^{total}}{Q_{H_2}^{film} \cdot Q_{H_2}^{plate} - Q_{H_2}^{film} \cdot Q_{H_2}^{total} - Q_{H_2}^{plate} \cdot Q_{H_2}^{total}} \tag{4}$$

Then, the hydrogen permeability coefficients P_{meas} of the different coating layers were calculated via normalization to a layer thickness of 1 µm, using their measured thickness values. The hydrogen permeation was measured at 0 %RH and at 0, 20, 60, and 80 °C to be able to calculate the activation energy E_A via an Arrhenius approach:

$$P_{meas}(T) = P_0 \cdot e^{-\frac{E_A}{RT}} \tag{5}$$

where $P_{meas}(T)$ is the permeability coefficient of the permeating gas at the respective temperature T, P_0 is the pre-exponential factor, and R is the universal gas constant.

2.3.7. Oxygen permeability coefficients

The oxygen permeance of the coated films was measured according to the DIN 53380-3 standard with the oxygen-specific carrier gas method [31]. The measurements were performed using an OX-TRAN 2/21 OTR Analyzer (AMETEK MOCON, Minneapolis, USA) at 20 °C and 0 %RH. Additional measuring temperatures used were 30 and 40 °C, also at a relative humidity of 0 %RH. The measurement was completed when the permeation stayed constant for at least 10 h. Duplicate determinations were performed for all of the coatings. The oxygen permeability coefficient P_{meas} was calculated similarly to the procedure used for helium. The oxygen permeance of the uncoated PET film ($Q_{O_2}^{film}$) was taken as 60.9 $\frac{cm^3\,(STP)}{m^2\,d\,bar}$. The activation energy for oxygen permeation was determined via Arrhenius correlation (Eq. (5)).

2.3.8. Water vapor permeability coefficients

The water vapor permeation rates of the coated films were measured according to the DIN EN ISO 15106-3 standard with the electrolytic detection sensor method [32]. The measurements were performed using an AQUATRAN Model 2 (AMETEK MOCON) at 23 °C and 80 %RH with twofold determinations. The measurement was completed as soon as the measured permeation rate stayed constant for at least 10 h. The water vapor permeability coefficient P_{meas} was calculated similarly to the procedure used for the other gases using the water vapor transmission rate of uncoated PET (8.4 $\frac{g\,(STP)}{m^2\,d}$) at 23 °C and 80 %RH.

2.3.9. Calculation of barrier improvement factor by particle integration

The theoretical barrier values were calculated according to the tortuous path approach for platelet-shaped particles. This approach was developed by Nielsen [25] and describes the barrier improvement of composites through the integration of impermeable platelets in the barrier layer. The elongation of the diffusion path is described by the tortuosity factor τ_{orig}:

$$\tau_{orig} = 1 + \frac{L}{2W} \cdot \eta_{MMT} \tag{6}$$

The aspect ratio of the MMT, i.e. the ratio of particle length L to particle thickness W, and the volume ratio of the silicate particles η_{MMT} define the tortuosity factor. In order to include the particle orientation in Nielsen's equation, Bharadwaj [33] suggested adding an order parameter S, leading to a modified tortuosity factor τ_{mod}. To obtain S, the average angle ζ between the particle plane and the substrate surface was determined as described in Section 2.3.4 from the pole figures of the composites:

$$S = \frac{1}{2} \cdot \left(3 \cdot \cos^2 \zeta - 1\right) \tag{7}$$

An order parameter of 1 ($\zeta = 0$) indicates a perfect perpendicular orientation. With the incorporation of S the tortuosity factor becomes:

$$\tau_{mod} = 1 + \frac{L}{2W} \cdot \eta_{MMT} \cdot \frac{2}{3} \cdot \left(S + \frac{1}{2}\right) \tag{8}$$

A further enhancement of Nielsen's equation, the squaring of the tortuosity factor, was suggested by Shen and Chen [34]. This leads to the following equation to calculate the theoretical permeability coefficients P_{cal} of the composites:

$$P_{cal} = \left(\frac{1 - \eta_{MMT}}{\left(1 + \frac{L}{2W} \cdot \eta_{MMT} \cdot \frac{2}{3} \cdot (S + \frac{1}{2})\right)^2} \right) \cdot P_{meas}^{ref} \tag{9}$$

Table 2
Density and surface energy with shares of polar and dispersive parts of the investigated polymer lacquers and the MMT dispersion before the mixing to produce composite lacquers. Water was included from Janczuk et al. [35] as a reference.

sample	density $\frac{g}{cm^3}$	surface energy $\frac{mN}{m}$	dispersive part	polar part
water	0.997	73	22	51
MMT-ref	1.032	68±0.8	41±0.6	27±0.2
PP-ref	0.949	52±0.4	38±0.2	14±0.2
PAD-ref	1.039	37±0.3	31±0.2	6.4±0.1
PCS-ref	1.041	68±0.4	34±0.2	35±0.2
PVA-ref	1.034	64±0.3	41±0.2	21±0.1

Here P_{meas}^{ref} are the measured permeability coefficients of the reference coating layers without particles. The values for L (494 nm) and W (25 nm) were taken from previous studies of the authors [19]. The volume ratio of the MMT particles with a density of 2.86 $\frac{g}{cm^3}$ is 12 vol% for 3:1 and 29 vol% for 1:1 mixing ratios. The measured (P_{meas}) and calculated (P_{cal}) permeability coefficients were compared according to:

$$\Delta = \left(\frac{P_{cal} - P_{meas}}{P_{cal}} \right) \quad (10)$$

If the value of the deviation Δ is positive, the measured value is lower than the calculated value, and vice versa. To evaluate the effect of the MMT particles on the barrier performance quantitatively, the barrier improvement factor BIF was used.

$$BIF = \frac{P_{meas}^{ref}}{P_{meas}^{comp}} \quad (11)$$

Here P_{meas}^{comp} is the measured permeability coefficient of the composite coating layers.

3. Results and discussion

3.1. Surface energies of coating liquids and dried coating surfaces

Table 2 shows the density and the surface energy, separated into dispersive and polar parts, of the polymer lacquers and the MMT dispersion before mixing to produce the composite lacquers. The total surface energy of the pure MMT dispersion having a solid content of 5 wt% was 68 $\frac{mN}{m}$. This value was in a similar range to the values for the polycarboxylic solution (PCS) and the polyvinyl alcohol solution (PVA) having surface energies of 68 and 64 $\frac{mN}{m}$, respectively. The polypropylene dispersion (PP) and the polyacrylic dispersion (PAD) provided lower values of 52 and 37 $\frac{mN}{m}$, respectively. Similar tendencies are valid for the polar parts.

When MMT is exfoliated in water, a hydration shell is built around the platelets, leading to swelling and further exfoliation of the particles [36]. This hydration shell is very sensitive to changes in the surface energy of the liquid [37]. It is therefore advantageous to mix liquids whose surface energy values differ as little as possible [38]. This difference between the surface energies of the lacquers and the MMT dispersion is lower for both PCS and PVA, whereas PP and PAD vary distinctly in total surface energy as well as in the polar part. PAD contained, for example, up to 2.5 wt% alcohols, which was the reason why the total surface energy was lower than that for a purely water-based system. For ethanol, Habib et al. [39] have shown that it displaces the hydration shell of MMT in the liquid state, which can cause re-agglomeration.

Before drying the composite lacquers, it is required to preserve the hydration shell around the MMT particles in order to maintain a homogeneous dispersion. During drying, the interaction of the polymer matrix and MMT becomes increasingly important since the water molecules evaporate and the hydration shells disappear [16]. Also in the dried state, it was again the case that PCS and PVA provided higher surface energies and also higher polarity parts than PP and PAD (Table 3). This indicates the potential for a stronger attraction between MMT and PCS or PVA.

Table 3
Surface energies of dispersive and polar components of the dried reference polymer and montmorillonite coating layers measured by the sessile drop method.

sample	surface energy	dispersive part	polar part
		$\frac{mN}{m}$	
MMT-ref	58±0.9	30±0.3	29±0.6
PP-ref	18±1.6	17±1.2	0.8±0.4
PAD-ref	31±1.2	31±1.2	0.1±0.0
PCS-ref	44±0.7	35±0.2	9.6±0.5
PVA-ref	43±1.0	39±0.6	4.2±0.4

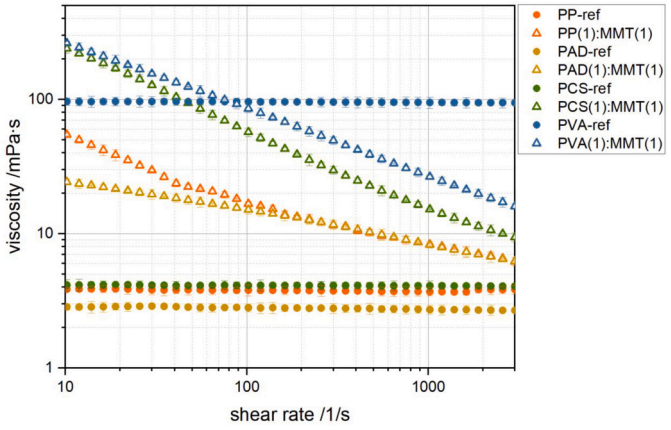


Fig. 2. Viscosity measurement of the polymer and composite lacquers with a mixing ratio of 1:1 as a function of shear rate.

3.2. Rheological investigation

Fig. 2 shows the viscosity of the polymer lacquers and composite lacquers with a mixing ratio of 1:1 by weight as a function of shear rate. When MMT is mixed into the polymer lacquers, the viscosities increase and the composite lacquers exhibit the shear-thinning behavior known for pure MMT dispersions [23,40]. The greater the shear-thinning, the stronger is the interaction between MMT and the polymer matrix [40].

The pure lacquers showed Newtonian behavior at the respective solid contents and measured shear rates. The viscosity increase due to the addition of MMT particles was much more pronounced for PCS (from 4.1 to 36 mPa s) than for PP (from 3.7 to 11 mPa s) or PAD (from 2.8 to 11 mPa s) at a shear rate of 10 $\frac{1}{s}$. The value of 47 mPa s at the same shear rate for PVA(1):MMT(1) also showed a distinct increase due to the addition of MMT. The slope indicates the shear-thinning effect. In this case, the strongest interaction between MMT and the polymer matrix was observed for PCS and PVA.

Similar measurements were carried out for the composite lacquers with a mixing ratio of 3:1 and confirmed this result (Fig. S1).

3.3. Fourier transform infrared spectroscopy

FTIR spectra were measured to examine interactions of polymer matrix material and MMT by identifying single peak shifts. According to Ellerbrock et al. [41], an unshifted peak in the composite spectra needs to be identified when analyzing peak shifts to eliminate the possibility of the whole curve being shifted. As shown in Table 4, every composite exhibits unshifted peaks of MMT and the polymer matrix.

Fig. 3 shows the FTIR spectra of the polymer (PP (A) and PAD (B)) layers, their composites with a mixing ratio of 1:1, and the MMT coating. No peak shifts were observed for composites comprising MMT and

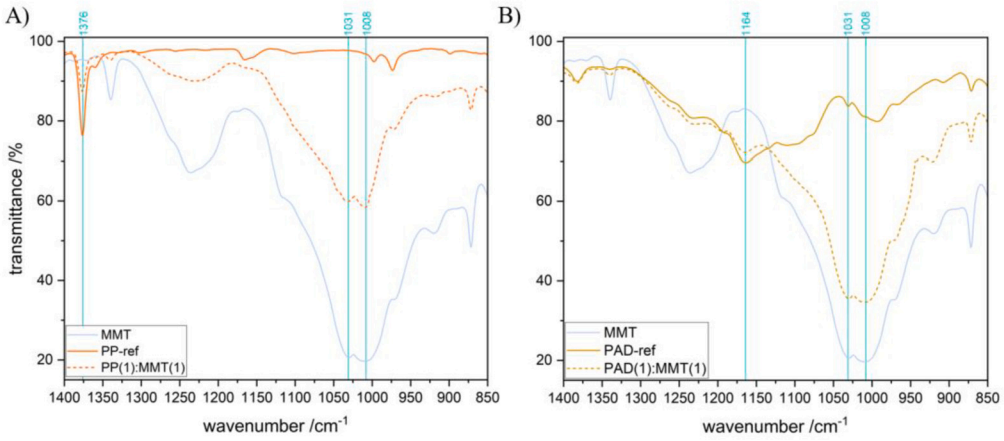


Fig. 3. FTIR spectra of montmorillonite, (A) PP-based and (B) PAD-based composites with a 1:1 mixing ratio of polymer and montmorillonite, and polymer coating layers zoomed in on the range from 1400 to 850 $\frac{1}{cm}$. The total spectrum in the range from 4000 to 600 $\frac{1}{cm}$ is shown in Fig. S2. The turquoise lines represent the unshifted bands indicating no interaction of MMT and polymer.

Table 4
Peak maxima with respective assignments of the polymer matrix materials used and the pure MMT coating layer. Peak shifts appearing in composites with a mixing ratio of 1:1 are assigned.

Material	Maxima ($\frac{1}{cm}$)	Assignment	Peak shift in composite
MMT [42]	3624	-OH stretching, Al-OH in octahedral sheets	no shift
	3425	-OH stretching, absorbed interlayer water	no shift
	1635	-OH bending, absorbed interlayer water	no shift
	1031	-Si-O stretching, Si-O-Si in tetrahedral sheets	blue-shift to 1041 $\frac{1}{cm}$ in PCS(1):MMT(1)
			blue-shift to 1037 $\frac{1}{cm}$ in PVA(1):MMT(1)
	1008	-Si-O stretching, Si-O-Si in tetrahedral sheets	blue-shift to 1018 $\frac{1}{cm}$ in PCS(1):MMT(1)
			blue-shift to 1016 $\frac{1}{cm}$ in PVA(1):MMT(1)
PP [43]	2950, 2867	-CH_3 stretching	no shift
	2919, 2840	-CH_2 stretching	no shift
	1457	-CH_2 bending	no shift
	1376	-CH_3 bending	no shift
PAD [44]	2922, 2849	-CH_2 stretching	no shift
	1730	-C=O stretching	no shift
	1164	-C-O stretching	no shift
PCS [45]	2942, 2832	-CH_2 stretching	no shift
	1713	-C=O stretching	red-shift to 1705 $\frac{1}{cm}$ in PCS(1):MMT(1)
	1092	-C-O stretching	red-shift to 1072 $\frac{1}{cm}$ in PCS(1):MMT(1)
PVA [46]	2933, 2910	-CH_2 stretching	no shift
	1709	-C=O stretching	no shift
	1085	-OH bending	red-shift to 1061 $\frac{1}{cm}$ in PVA(1):MMT(1)

PP. These peaks at 1457 and 1376 $\frac{1}{cm}$ for PP and at 3624 and 1031 $\frac{1}{cm}$ for MMT are similar to those identified previously for PP and MMT based barrier coating layers [47–49]. PP does not provide any functional group with which an interaction with MMT might be possible.

For PAD-based composites, no peak shifts were observed. Compared with PP, an interaction with PAD would be possible in the form of hydrogen bonds with the carbonyl or the ether group of the acrylate. However, these bands stayed unshifted, which indicates that these functional groups are not accessible for interaction with the MMT. Ianchis et al. [50] also observed no peak shifts for composite coating layers with non-modified MMT and polyacrylates.

Fig. 4 shows the FTIR spectra of the polymer layers (PCS (A) and PVA (B)), their composites with a mixing ratio of 1:1, and the MMT coating layer. Peak shifts were identified for both composites. The -C-O stretching band from the carboxylic acid exhibited a red shift when mixed with MMT, as also observed by Smith [51]. Similar red shifts for the -C-O stretching band of the carboxyl group have also been found by Lai et al. [52], Natkański et al. [53], and Yu et al. [54] in composites of polycarboxylic acid and MMT. In addition, the band of the Si-O stretching vibration in MMT showed a blue shift. These peak shifts indicate an interaction of the Si-O group from the Si-tetrahedral layer of MMT with the hydroxy group from the carboxyl group of the carboxylic acid, most likely via hydrogen bonds [55,56].

Similarly to PCS, for PVA composites band shifts also appear for O-H bending and Si-O stretching vibrations of MMT, shown by red and blue colors, respectively. This kind of red shift for the hydroxy group in PVA was also observed by Spoljaric et al. [57] for composites comprising PVA and MMT.

3.4. Pole figures

Fig. 5 shows the average intensity of the MMT 001 peak as a function of tilt angle for the MMT-ref sample and the composite coatings with a mixing ratio of 1:1 based on the pole figure measurements.

The peak shape and position indicate the orientation of the silicate platelets in the coating layer. All peaks provide their maximum at 0°, which suggests that the average orientation is parallel to the surface. The narrower the peak is, the more particles are oriented parallel to

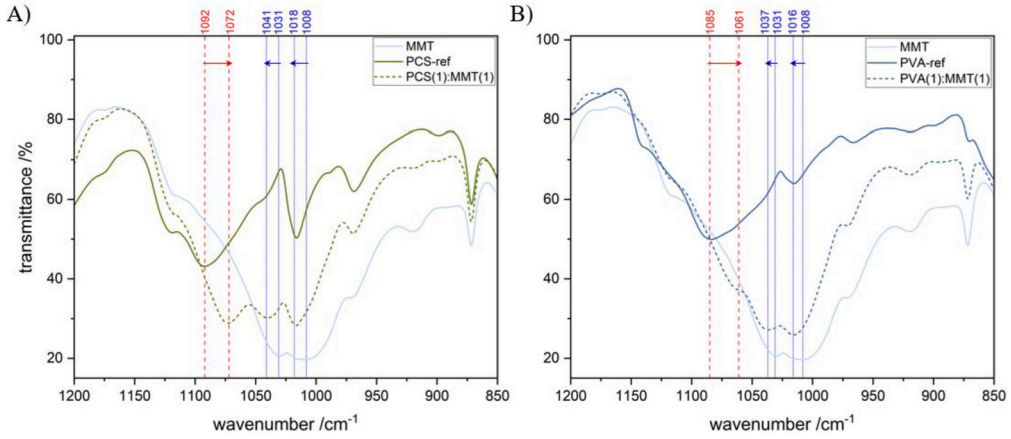


Fig. 4. FTIR spectra of montmorillonite, (A) PCS-based and (B) PVA-based composites with a 1:1 mixing ratio of polymer and montmorillonite, and polymer coating layers zoomed in on the range from 1200 to 850 $\frac{1}{cm}$. The total spectrum in the range from 4000 to 600 $\frac{1}{cm}$ is shown in Fig. S3. The red and blue represent peak shifts indicating interaction between MMT and the polymer.

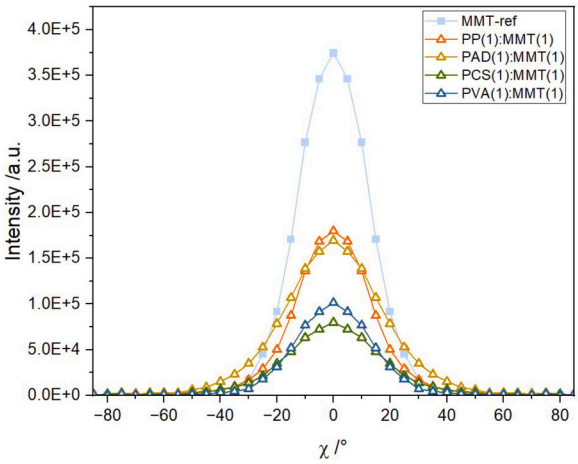


Fig. 5. Average intensity over all rotation angles ϕ from 0 to 360° plotted against the tilt angle χ for the MMT-ref samples and composite coatings with a mixing ratio of 1:1. The underlying pole figures are shown in Figs. S16-S19.

Table 5
Calculated integral breadth and alignment angle for the MMT-ref sample and all composite coatings with mixing ratios of 1:1 and 1:3.

sample	integral breadth	alignment angle ζ (°)
MMT-ref	30	8.32
PP(3):MMT(1)	39	18.4
PP(1):MMT(1)	37	17.7
PAD(3):MMT(1)	45	23.2
PAD(1):MMT(1)	41	20.4
PCS(3):MMT(1)	35	14.2
PCS(1):MMT(1)	34	14.0
PVA(3):MMT(1)	33	11.5
PVA(1):MMT(1)	33	10.6

the substrate surface since the measurement signals indicate the (001) lattice plane, which is the plane perpendicular to the area of the plate. The numerical value describing the peak width is the integral breadth listed in Table 5. The smaller the integral breadth is, the more particles are aligned parallel to the surface.

The particles in the MMT-ref coating layer were aligned the most parallel, followed by the PVA- and PCS-based composite coatings. The orientation became less parallel for PP-based coatings and coating layers based on PAD provided the most heterogeneous alignment.

When coating the pure MMT dispersion, the water molecules do not disturb the platelets from their physically driven behavior to lie parallel to the surface when the solid content of the dispersion is low enough [58]. The shearing during coating even forces the particles to orient parallel to the surface. Adding a polymer as a third ingredient to the lacquer, in addition to MMT and water, impeded the orientation of the platelets. As the PP and PAD lacquers are dispersions, the polymer chains are not dissolved in water, but the polymers are distributed in spherical form and only liquefy during the coating and drying process. The spherical shape of these polymers in water and the fact that particle liquefaction only takes place after shearing could be a reason why the orientation of the particles in PP and PAD was less parallel, as the polymer spheres act as obstacles during application of the coating (Fig. S7-S9). PCS and PVA are solutions, i.e., the polymer chains are completely dissolved in water and embedded between the MMT particles during the coating. This matches on the one hand the steeper slopes of PCS- and PVA-based composites in the viscosity measurements (Fig. 2), which indicate a more pronounced interaction due to the stronger shear-thinning effect. On the other hand, it matches the findings of peak shift investigations in Section 3.3: the interaction of MMT with the polymers, PCS and PVA. A similar investigation, confirming the results, was performed for composite coating layers with mixing ratios of 3:1 (Figs. S16-S20).

The pole figures were also used to determine the alignment angle ζ, which was used to calculate the order parameter S according to Eq. (7). Fig. 6 shows the influence of the alignment angle on the modified tortuosity factor. A change in the particle volume fraction affects the tortuosity more than the alignment angle. The orientation in the investigated composites varies within a range of only 10.6 to 23.2°, leading to a small effect on the tortuosity factor and therefore the permeability coefficients.

3.5. Helium barrier

Fig. 7A shows the values for the helium permeability coefficients of the coating layers.

P_{meas} for helium of the PP-ref sample was 3.7×10^4 $\frac{cm^3\,(STP)\,1\,\mu m}{m^2\,d\,bar}$ and decreased to 1.7×10^3 $\frac{cm^3\,(STP)\,1\,\mu m}{m^2\,d\,bar}$ when mixed with 50 wt% MMT. This corresponds to a BIF of 21. It has been shown previously that the helium permeability of PP can be reduced by the addition MMT [59,60]. In these previous studies, the MMT was added to PP melt, which is why the amount of MMT was limited to 6 wt%. Hence the BIFs obtained were below 2. The addition of MMT to the aqueous PP dispersion in this study allowed an MMT content of up to 50 wt% in the composite barrier layers. This system was examined for the first time to the best

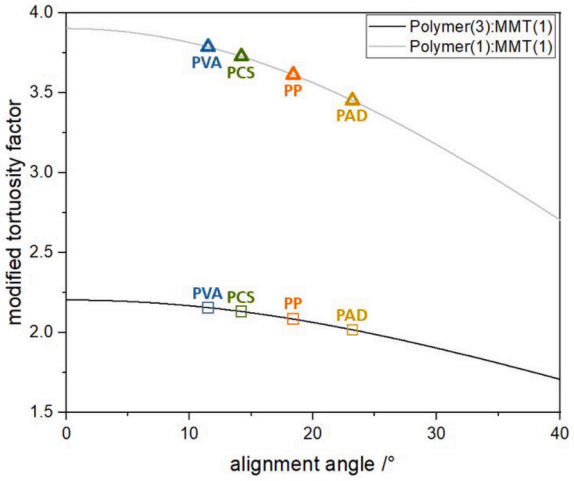


Fig. 6. The black and gray lines show the values of the modified tortuosity factor τ_{mod} calculated according to Eq. (8) for alignment angles ζ from 0 to 40°. The measured alignment angles for the investigated composites from Table 5 are marked for the respective polymer matrices.

of the authors' knowledge. The calculated permeability coefficient P_{cal} according to Eq. (9) was 2.0×10^3 $\frac{cm^3\,(STP)\,1\,\mu m}{m^2\,d\,bar}$. The 11 % deviation between the calculated and the experimentally measured values according to Eq. (10) for PP(1):MMT(1) indicates that the composite performed better than predicted. The calculation used only takes geometrical parameters (such as orientation, particle volume ratio, and aspect ratio) into account and differences in the polymer matrix possibly induced by the MMT are not considered. These differences might be changes in the free volume of the polymer matrix or variations in the crystallinity of the polymer, for example. The XRD pattern (Fig. S21A) of PP-ref and PP(1):MMT(1) showed no distinct variation in the crystallinity of PP due to the addition of MMT. The integration of MMT in the PP matrix might have reduced the free volume slightly in PP and therefore reduced the helium permeation in addition to the tortuosity. The phenomenon of free volume reduction in PP matrix systems on addition of MMT was also observed by Hu et al. [61].

The composites with the PAD matrix showed low BIFs. Since the orientation factors of the MMT in PP and PAD did not differ substantially, the BIFs could be expected to be in the same range. The fact that this is not the case proves that not only the addition of MMT, but also the interaction of MMT with the matrix, the homogeneous distribution, and the influence of the particles on the polymer matrix are important to consider. The calculated P_{cal} for the 1:1 mixture with PAD (8.9×10^2 $\frac{cm^3\,(STP)\,1\,\mu m}{m^2\,d\,bar}$) deviated considerably from the measured P_{meas} (3.3×10^3 $\frac{cm^3\,(STP)\,1\,\mu m}{m^2\,d\,bar}$) with a value of −272 %. The fact that the deviation is negative implies that the particles did not exert their full potential for the He barrier enhancement of the PAD matrix. It is more likely that the particles re-agglomerate when mixed with PAD since the surface energies of PAD lacquer and MMT dispersion differed, as discussed in Section 3.1. From an energetic point of view, a re-agglomeration of particles appears to be favorable in PAD, since neither the viscosity values of its composite lacquers nor the FTIR spectra of the dried composite coating layers indicate an interaction between the two materials. The XRD pattern (Fig. S21B) revealed an increased crystallinity of PAD in the composite coating layers since peaks appear in the range from 10 to 25° compared with PAD-ref. An increase in crystallinity leads to an increase in gas barrier [62]. However, it seems that the re-agglomeration of particles outperformed the increase in crystallinity with respect to barrier properties.

P_{meas} for helium of the PCS-ref sample was measured as 3.7×10^2 $\frac{cm^3\,(STP)\,1\,\mu m}{m^2\,d\,bar}$, which decreased to 7.8 $\frac{cm^3\,(STP)\,1\,\mu m}{m^2\,d\,bar}$ when 50 wt% MMT was added. This corresponds to a barrier improvement factor of 47. Tzeng et al. [63] reported a helium permeance of 4.1 $\frac{cm^3\,(STP)}{m^2\,d\,bar}$ for 10 alternating layers of polyethylenimine, poly(acrylic acid), and MMT with a total layer thickness of 1.6 µm. Herrera-Alonso et al. [64] investigated composites of polybutylmethacrylate with MMT and obtained a BIF of 1.3 for helium with an MMT content of 5 wt%. The higher MMT content is one reason for the higher BIFs in this study. The aqueous lacquers used made it possible to dilute the mixture and thus keep the viscosity in a processable range, even with MMT-rich mixing ratios such as 1:1. The reason for the positive deviation of 58 % from the calculated (1.9×10^1 $\frac{cm^3\,(STP)\,1\,\mu m}{m^2\,d\,bar}$) to the measured (7.9 $\frac{cm^3\,(STP)\,1\,\mu m}{m^2\,d\,bar}$) values for PCS(1):MMT(1) is changes in the polymer matrix. The results reported in Sections 3.1 and 3.3 indicate an interaction between the PCS matrix and the MMT which may have led to a reduced free volume and therefore a better barrier. Additionally, the integration of MMT increased the crystallinity of the PCS matrix (Fig. S22A), which also should lead to an improvement in its gas barrier.

The findings for PVA-based composites are very similar to those for PCS-based composites. The BIFs of 12 and 49 for 3:1 and 1:1 mixing ratios, respectively, were in the same range as for PCS. The PVA molecule also has an accessible hydroxy group that interacts with the Si-O group from the MMT's silicate tetrahedra via hydrogen bonds, similarly to the carboxylic acid's functional group of PCS. That this interaction occurred was concluded from the FTIR spectra in Fig. 4. The XRD pattern (Fig. S22B) indicated also for PVA an increase in crystallinity due to the integration of MMT. Barrier layers of composites comprising PVA and MMT have been well investigated for barrier applications owing to their good compatibility [19,65–67]. A very low P_{meas} of 8.0×10^{-1} $\frac{cm^3\,(STP)\,1\,\mu m}{m^2\,d\,bar}$ was reported by Habel et al. [68] for composite coating layers comprising PVA and synthetic clay sodium fluorohectorite particles applied with multiple layer spray coating. In previous studies, the authors reported a BIF of 17 for a coating layer with a similar composition of 1:1 on oriented PP substrate film [19]. The reason for the observed difference in the BIFs for the same coating lies in the substrate film. The PET used in this study is thermally and mechanically more robust than PP and induces lower stress in the coating layer.

3.6. Hydrogen barrier

The general trends found for helium permeation were also valid for hydrogen permeation, as shown in Fig. 7B. The deviations from the calculated values were positive for PP-, PCS-, and PVA-based coatings and negative for PAD-based coatings for similar reasons. The BIFs for composite coating layers with a 3:1 mixing ratio were constantly lower than the BIFs for coating layers with a 1:1 mixing ratio. The highest BIFs were reached for PCS(1):MMT(1) and PVA(1):MMT(1) with values of 37 and 41, respectively.

Comparing the measured hydrogen and helium permeability coefficients shows the trend that the values of P_{meas} for hydrogen were slightly lower than those for helium. The reason for this is that the helium atom is smaller than the hydrogen molecule in terms of the gas kinetic diameter, while both gases are non-polar [24]. Smaller permeating particles find more permeation paths, therefore the value for the permeability coefficient is higher (Fig. 9). Consequently, the BIFs measured for helium were slightly higher than those for hydrogen, because the generation of an obstacle to permeation, an MMT particle, has a greater influence for smaller permeants.

The permeation of hydrogen through silicate-based composites was investigated previously. Tzeng et al. [63] reported a hydrogen permeance of 3.7 $\frac{cm^3\,(STP)}{m^2\,d\,bar}$ for 10 alternating layers of polyethyleneimine, poly(acrylic acid), and MMT with a total layer thickness of 1.6 µm. In comparison, a value of 9.3×10^{-1} $\frac{cm^3\,(STP)\,1\,\mu m}{m^2\,d\,bar}$ was obtained with a one-time coating in this study with PCS(1):MMT(1). A very low P_{meas} of 6.0×10^{-1} $\frac{cm^3\,(STP)\,1\,\mu m}{m^2\,d\,bar}$ was reported by Habel et al. [68] for composite

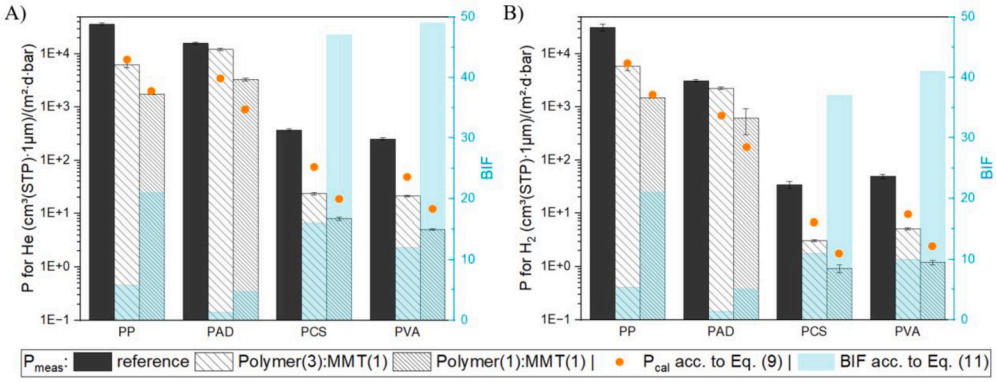


Fig. 7. Helium (A) and hydrogen (B) permeability coefficients of the coating layers of the four different polymer matrices (PP, PAD, PCS, and PVA) and their composites with mixing ratios of 3:1 and 1:1 with MMT. The measurement conditions for helium and hydrogen permeability were 23 °C/0 %RH and 20 °C/0 %RH, respectively. The orange dots represent the P_{cal} values according to Eq. (9). The transparent blue bars show the barrier improvement factors ($BIFs$) for the respective mixing ratio according to Eq. (11) (right y-axis).

Table 6
Activation energies for hydrogen and oxygen permeation of the reference and composite coating layers. The respective Arrhenius plots are shown in Figs. S23 to S26.

sample	hydrogen $\frac{kJ}{mol}$	oxygen
PP-ref	30.4	30.7
PP(3):MMT(1)	30.9	30.2
PP(1):MMT(1)	29.9	30.2
PAD-ref	21.6	30.5
PAD(3):MMT(1)	23.1	29.7
PAD(1):MMT(1)	24.4	28.6
PCS-ref	42.2	29.3
PCS(3):MMT(1)	39.3	24.5
PCS(1):MMT(1)	36.8	20.6
PVA-ref	47.5	56.5
PVA(3):MMT(1)	45.1	49.8
PVA(1):MMT(1)	39.5	45.8

layers comprising PVA and synthetic clay sodium fluorohectorite particles applied with multiple layer spray coating. The lowest permeability coefficient for hydrogen measured for a single-layer PVA-based composite was 1.2 $\frac{cm^3\,(STP)\,1\,\mu m}{m^2\,d\,bar}$ in their study. Kim et al. [69] recently published a hydrogen permeance of 6.5×10^{-3} $\frac{cm^3\,(STP)}{m^2\,d\,bar}$ at 23 °C for a composite coating comprising MMT and polyvinylpyrrolidone (PVP). The coating with a composition of 63 wt% MMT and 37 wt% PVP was applied on a nylon substrate at a layer thickness of 60 µm. The 63 wt% MMT concentration and the coating layer thickness are the reasons for its higher barrier performance.

In addition to the measurements at 20 °C, the permeation of hydrogen was measured at 0, 60, and 80 °C to calculate the activation energy for permeation according to Eq. (5) (Table 6). The Arrhenius plots for hydrogen and oxygen are linear, indicating no structural changes occurring in the composites, such as hydrogenation or oxidation possibly induced by these gases [70]. It is notable that the activation energy for permeation hardly changed for the two polymer matrices, PP and PAD, with the addition of MMT. For the two polymer matrices, PCS and PVA, where an interaction with MMT was observed, the values of E_A decreased with increasing MMT content.

Kim and Lin [71] have shown that a change in E_A indicates a change in the permeation mechanism. The mechanism of permeation through a pure polymer coating is considered linear and determined by the properties of the polymer matrix [25]. The addition of MMT to the polymer changes the matrix in such a way that boundary areas between MMT and the polymer are created. Erlat et al. [72] showed that the permeation mechanism of gases might occur along these boundary areas, which are not as dense as in the bulk of the matrix because of the shown interaction between MMT and the polymer matrix. The fact that a reduced E_A is measured for the samples with the lowest permeation coefficient indicates that the tortuosity has more influence on the permeation coefficient than changes in the polymer matrix.

3.7. Oxygen barrier

The results for P_{meas} for oxygen followed the trends that were observed for helium and hydrogen permeation (Fig. 8A). The $BIFs$ for a 3:1 mixing ratio were constantly lower than those for a 1:1 mixing ratio. The deviations of the measured values from the calculated values according to Eq. (10) were positive for PP-, PCS-, and PVA-based coating layers and negative for PAD-based coating layers for the aforementioned reasons. The overall best barriers were achieved for PCS- and PVA-based composites with a mixing ratio of 1:1.

The oxygen molecule was the largest permeating non-polar gas compared with the helium atom and the hydrogen molecule, which consequently led to the lowest permeability coefficients (Fig. 9). This is exemplified by the permeability coefficients of the PVA-ref samples. The coefficient for helium was 2.5×10^2 $\frac{cm^3\,(STP)\,1\,\mu m}{m^2\,d\,bar}$, that for hydrogen was 4.9×10^1 $\frac{cm^3\,(STP)\,1\,\mu m}{m^2\,d\,bar}$, and that for oxygen was 1.1×10^{-1} $\frac{cm^3\,(STP)\,1\,\mu m}{m^2\,d\,bar}$. After adding 50 wt% MMT, the coefficients decreased to 5.1 $\frac{cm^3\,(STP)\,1\,\mu m}{m^2\,d\,bar}$ for helium, 1.2 $\frac{cm^3\,(STP)\,1\,\mu m}{m^2\,d\,bar}$ for hydrogen, and 4.2×10^{-3} $\frac{cm^3\,(STP)\,1\,\mu m}{m^2\,d\,bar}$ for oxygen.

Table 6 shows the activation energies for oxygen permeation. The values of E_A showed no substantial changes for PP- and PAD-based polymer matrices when MMT particles were added to the lacquer recipe. For the PCS- and PVA-based composites the values of E_A decreased with increasing MMT content. Hence it is also valid for oxygen that the permeability coefficient decreases with integration of MMT even if the activation energy for permeation decreases. This indicates that even when the energy for permeation along a diffusion path is reduced, the elongation of the diffusion path is the determining factor for the resulting permeability coefficients.

3.8. Water vapor barrier

It is immediately apparent that the trends observed for the non-polar gases differ considerably for water vapor (Fig. 8B). The y-axis is no longer logarithmically scaled. The BIF values are now very low for all polymer matrices, not only for PAD-based coatings. All measured permeability coefficient deviate strongly from the calculated values. For

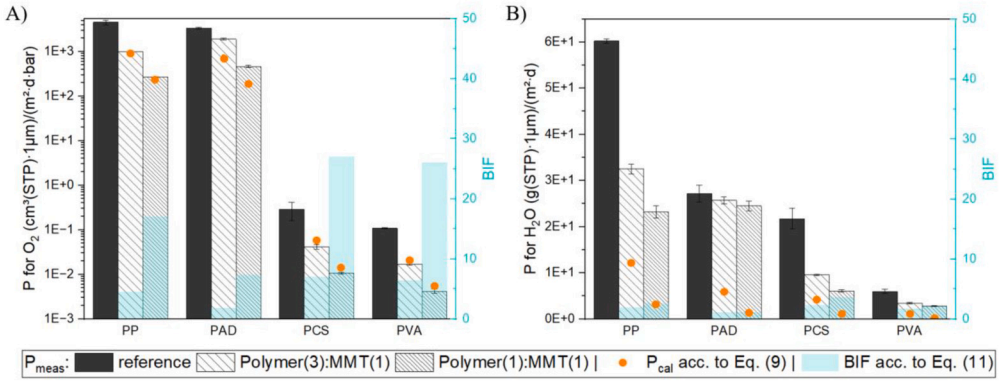


Fig. 8. Oxygen (A) and water vapor (B) permeability coefficients of the coating layers of the four different polymers (PP, PAD, PCS, and PVA) and their composites with mixing ratios of 3:1 and 1:1 with MMT. The measurement conditions for oxygen and water vapor permeability were 23 °C/50 %RH and 23 °C/80 %RH, respectively. The orange dots represent the P_{cal} values according to Eq. (9). The transparent blue bars show the barrier improvement factors (BIFs) for the respective mixing ratio according to Eq. (11) (right y-axis).

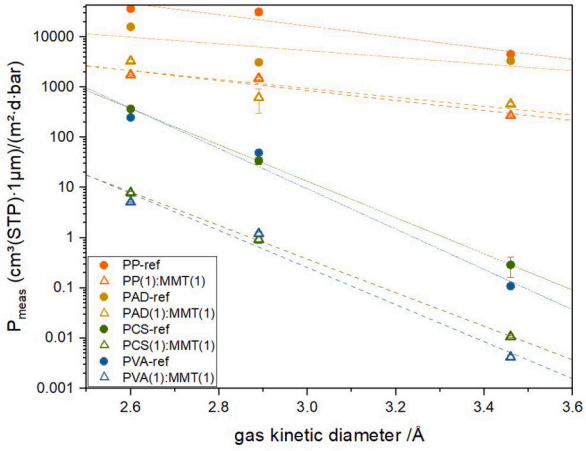


Fig. 9. Permeability coefficients as a function of the gas kinetic diameter for helium (2.60 Å), hydrogen (2.89 Å), and oxygen (3.46 Å). The dotted (reference coatings) and dashed (mixing ratio of 1:1) linear trend lines plotted for the reference and composite coatings, respectively, indicate the correlation between the gas permeability coefficients and gas kinetic diameter.

example, the BIFs of PVA composites with mixing ratios of 3:1 and 1:1 were 6.4 and 26 for oxygen and only 1.9 for water vapor in both cases. Indeed, the measured BIFs for the 3:1 and 1:1 mixing ratios were in the same range for all the matrix materials. This indicates that the permeability of water vapor through composites with MMT are not primarily determined by the tortuosity as is the case for the non-polar gases. The barrier performance of the coating layers against the non-polar gases was additionally supported by changes in the polar matrix, as indicated by the positive deviation values. For water vapor permeation, the BIF values did not differ significantly between the polymer matrices and the values were distinctly lower than expected due to tortuosity. This indicates that even when the particles were distributed homogeneously, which was the case for PP, PCS, and PVA, the possible barrier improvement due to tortuosity was not achieved. Water vapor was the only polar permeant investigated in this study regarding permeability through the composites. MMT also has a high polarity. The similarity of their polarities is one of the reasons why the MMT particles are permeable to the small water molecules (2.65 Å), and the MMT particles might absorb the water molecules. The phenomenon that the absorption of water molecules takes place from MMT particle to MMT particle in the permeation direction was suggested to be called the "polar path effect" by Sankaran et al. [73] and was already described by Nielsen [25]. The permeation of water molecules along these polar paths is assumed to be induced by capillary driving forces next to the concentration gradient [74,75]. Due to its absorption property, the solubility coefficient for water vapor increased in composites when MMT was added to the polymer matrices [76].

The abovementioned permeation mechanism for water vapor, which is not dominated by the tortuous path effect, is the reason why BIFs in silicate-based polymer composites are usually quite low [77,78], as also observed in this study.

4. Conclusion

Composite barrier lacquers based on platelet-shaped MMT and aqueous polymer lacquers were prepared. The polymer matrix materials tested were polypropylene (PP), polyacrylate (PAD), polycarboxylic acid (PCS), and polyvinyl alcohol (PVA). The prepared composite lacquers were coated on PET films and the barrier properties against helium, hydrogen, oxygen, and water vapor were investigated.

The study aimed to investigate the influencing factors for gas and water vapor permeation through the coated films. These factors include the interaction between the polymer matrix and MMT, the orientation of the MMT particles in the coating layer, the change in polymer crystallinity due to its mixing with particles, the permeant type, and the tortuosity. The effect of the tortuosity factor was investigated by comparison of calculated and measured values of permeation, while the calculations were based on the tortuous path theory developed by Nielsen [25].

It was found that the addition of MMT to the aqueous polymers increases the viscosity of the lacquers and adds a shear-thinning property. The shear-thinning effect at shear rates from 3 to 3000 $\frac{1}{s}$ was most pronounced for composites with PVA (reduction of viscosity from 479 to 16.0 mPa s) and PCS (from 680 to 9.39 mPa s), indicating the strongest interaction for those polymer matrices with MMT in the liquid state. For the dried state, it was confirmed via peak shifts in the FTIR spectra that the interaction of MMT and polymer in the form of hydrogen bonds is only apparent for PCS and PVA. These two polymer matrices are indeed the ones in which the orientation of the platelets was more parallel (alignment angle of 10.6 to 14.2°) to the surface in comparison with PP and PAD (alignment angle of 17.7 to 23.2°). For PP- and PAD-based composites, no indication of interaction with MMT was found. Consequently, the barrier properties of PCS- and PVA-based composites outperformed those of the PP- and PAD-based composites. The helium permeability coefficients of the 1:1 mixtures of polymer and MMT for PP and PVA, which are 1.7×10^3 and 5.1 $\frac{cm^3\,(STP)\,1\,\mu m}{m^2\,d\,bar}$, respectively, are given here as examples. These correspond to barrier improvement factors of 21 and 49 for PP and PVA, respectively, when 50 wt% MMT are added to the coating layer. The permeability coefficients were found to be highest for the smallest permeant, the helium. The deviation from

the calculated values was found to be highest for the smallest permeants, helium and hydrogen. The fact that the deviation was found to be positive in the case of PP, PCS, and PVA matrix materials indicates that the addition of MMT not only leads to an elongated diffusion path but also to advantageous changes in the polymer matrix, leading to an even better barrier performance than predicted.

The findings in this study expand the understanding of mechanisms of permeation through composite coating layers and will be of help in developing applications for this technology of wet composite barrier coatings. The coating formulations are to be adapted according to the requirements towards gas barrier, flexibility, sealability, or moisture resistance. The results of this study provide guidelines on how the gas barrier of the coating layer can be improved. If the requirements allow a high MMT concentration (up to 50 wt%), it is advisable to use water-based coatings, which gives the possibility to integrate MMT at higher concentrations. The MMT content has a stronger effect on the barrier of the coating layer than the orientation of the particles. It is also recommended to have polymer matrices with a surface energy of above 50 $\frac{mN}{m}$ (polar content above 20 $\frac{mN}{m}$), as this opens up the possibility of interactions with MMT.

Funding

This work has received funding from the European Union's Horizon 2020 research and innovation program under grant agreement n°862156 FlexFunction2Sustain project.

CRediT authorship contribution statement

Stefan Schiessl: Writing – review & editing, Writing – original draft, Validation, Methodology, Investigation, Data curation, Conceptualization. **Esra Kucukpinar:** Investigation, Funding acquisition, Conceptualization, Methodology, Supervision, Validation, Writing – review & editing. **René Schwiddessen:** Data curation, Investigation, Methodology, Resources, Validation. **Horst-Christian Langowski:** Conceptualization, Methodology, Supervision, Validation, Writing – review & editing. **Peter Eisner:** Conceptualization, Methodology, Supervision, Writing – review & editing.

Declaration of competing interest

The authors declare that they have no known competing financial interests or personal relationships that could have appeared to influence the work reported in this paper.

Data availability

The data presented in this study are available on request from the corresponding author. The data are not publicly available for reasons of confidentiality in the aforementioned EU project, see section "Funding".

Acknowledgements

The authors sincerely thank Ms. Ines Pietsch of BASF, Mr. Hanns Misiak of Henkel, Mr. Samuel Michel of Kuraray, and Mr. Leon Krings of Paramelt, who provided the samples and supported in the form of discussions. Hans Ewender of Fraunhofer IVV is acknowledged for performing the hydrogen barrier measurements. Stephané Cros of CEA Tech is acknowledged for the execution of the helium barrier measurements.

Appendix A. Supplementary material

Supplementary material related to this article can be found online at https://doi.org/10.1016/j.surfcoat.2024.130800.

References

[1] A. Arora, G. Padua, Review: nanocomposites in food packaging, J. Food Sci. 75 (1) (2010) R43–R49, https://doi.org/10.1111/j.1750-3841.2009.01456.x.
[2] M. Manceau, A. Rivaton, J.-L. Gardette, S. Guillerez, N. Lemaître, The mechanism of photo- and thermooxidation of poly(3-hexylthiophene) (P3HT) reconsidered, Polym. Degrad. Stab. 94 (6) (2009) 898–907, https://doi.org/10.1016/j.polymdegradstab.2009.03.005.
[3] K. Choi, S. Nam, Y. Lee, M. Lee, J. Jang, S.J. Kim, Y.J. Jeong, H. Kim, S. Bae, J.-B. Yoo, S.M. Cho, J.-B. Choi, H.K. Chung, J.-H. Ahn, C.E. Park, B.H. Hong, Reduced water vapor transmission rate of graphene gas barrier films for flexible organic field-effect transistors, ACS Nano 9 (6) (2015) 5818–5824, https://doi.org/10.1021/acsnano.5b01161, pMID: 25988910.
[4] M. Muthukumar, N. Rengarajan, B. Velliyangiri, M. Omprakas, C. Rohit, U. Kartheek Raja, The development of fuel cell electric vehicles – a review, Mater. Today Proc. 45 (2021) 1181–1187, https://doi.org/10.1016/j.matpr.2020.03.679, International Conference on Advances in Materials Research - 2019.
[5] M. Mariello, K. Kim, K. Wu, S.P. Lacour, Y. Leterrier, Recent advances in encapsulation of flexible bioelectronic implants: materials, technologies, and characterization methods, Adv. Mater. 34 (34) (2022) 2201129, https://doi.org/10.1002/adma.202201129.
[6] N. Liu, J. Zheng, D.B. Bogy, Thermal flying-height control sliders in hard disk drives filled with air-helium gas mixtures, Appl. Phys. Lett. 95 (21) (2009), https://doi.org/10.1063/1.3268468.
[7] S.-H. Schulze, C. Ehrich, R. Meitzner, M. Pander, Helium permeation as a fast quality indicator for barrier properties of solar cell encapsulates, Prog. Photovolt. 25 (12) (2017) 1051–1058, https://doi.org/10.1002/pip.2922.
[8] F. Herbst, S. Großer, P.C. With, L. Prager, M. Pander, Helium transmission rate as a rapid and reliable method for assessing the water vapour transmission rate of transparent PET-SiOx barrier foils, Packag. Technol. Sci. 34 (8) (2021) 497–504, https://doi.org/10.1002/pts.2576.
[9] K. Miller, J. Krochta, Oxygen and aroma barrier properties of edible films: a review, Trends Food Sci. Technol. 8 (7) (1997) 228–237, https://doi.org/10.1016/S0924-2244(97)01051-0.
[10] C. Charton, N. Schiller, M. Fahland, A. Holländer, A. Wedel, K. Noller, Development of high barrier films on flexible polymer substrates, Thin Solid Films 502 (1) (2006) 99–103, https://doi.org/10.1016/j.tsf.2005.07.253, Selected Papers from the 5th International Conference on Coatings on Glass (ICCG5) - Advanced Coatings on Glass and Plastics for Large-Area or High-Volume Products.
[11] M.A. Priolo, K.M. Holder, T. Guin, J.C. Grunlan, Recent advances in gas barrier thin films via layer-by-layer assembly of polymers and platelets, Macromol. Rapid Commun. 36 (10) (2015) 866–879, https://doi.org/10.1002/marc.201500055.
[12] S. Kiese, E. Kücükpinar, O. Miesbauer, H.-C. Langowski, Time-dependent water vapor permeation through multilayer barrier films: empirical versus theoretical results, Thin Solid Films 672 (2019) 199–205, https://doi.org/10.1016/j.tsf.2019.01.001.
[13] J.G. Acheson, A. McFerran, D. Xu, M. Ziminska, S. Goel, A.B. Lennon, N. Dunne, A.R. Hamilton, Hydrated behavior of multilayer polyelectrolyte-nanoclay coatings on porous materials and demonstration of shape memory effect, Surf. Coat. Technol. 458 (2023) 129335, https://doi.org/10.1016/j.surfcoat.2023.129335.
[14] T. Gulin-Sarfraz, M.S. Grøvlen, E. Rosqvist, M.K. Pettersen, J. Peltonen, J. Sarfraz, Optimized multilayer coating using layer-by-layer assembly method for excellent oxygen barrier of poly(lactic acid) based film, Colloids Surf. A, Physicochem. Eng. Asp. 664 (2023) 131155, https://doi.org/10.1016/j.colsurfa.2023.131155.
[15] B. Tan, N. Thomas, A review of the water barrier properties of polymer/clay and polymer/graphene nanocomposites, J. Membr. Sci. 514 (2016) 595–612, https://doi.org/10.1016/j.memsci.2016.05.026.
[16] S.-L. Bee, M. Abdullah, S.-T. Bee, L.T. Sin, A. Rahmat, Polymer nanocomposites based on silylated-montmorillonite: a review, Prog. Polym. Sci. 85 (2018) 57–82, https://doi.org/10.1016/j.progpolymsci.2018.07.003.
[17] L. Alves, E. Ferraz, J. Gamelas, Composites of nanofibrillated cellulose with clay minerals: a review, Adv. Colloid Interface Sci. 272 (2019) 101994, https://doi.org/10.1016/j.cis.2019.101994.
[18] A. Cabrini, A. Ghalayani Esfahani, A. Petraconi, M. Lavorgna, L. De Nardo, G.G. Buonocore, R.J.E. Andrade, P. Cerruti, Ultrasonic spray deposition of PEGDE-crosslinked chitosan/graphene oxide coatings for enhancing gas barrier properties of polybutylene succinate films, Prog. Org. Coat. 183 (2023) 107760, https://doi.org/10.1016/j.porgcoat.2023.107760.
[19] S. Schiessl, E. Kucukpinar, S. Cros, O. Miesbauer, H.-C. Langowski, P. Eisner, Nanocomposite coatings based on polyvinyl alcohol and montmorillonite for high-barrier food packaging, Front. Nutr. 9 (2022), https://doi.org/10.3389/fnut.2022.790157.
[20] G. Zehetmeyer, R.M.D. Soares, A. Brandelli, R.S. Mauler, R.V.B. Oliveira, Evaluation of polypropylene/montmorillonite nanocomposites as food packaging material, Polym. Bull. 68 (8) (2012) 2199–2217, https://doi.org/10.1007/s00289-012-0722-1.
[21] M. Sirousazar, M. Yari, B.F. Achachlouei, J. Arsalani, Y. Mansoori, Polypropylene/montmorillonite nanocomposites for food packaging, e-Polymers 7 (1) (2007) 027, https://doi.org/10.1515/epoly.2007.7.1.305.
[22] J. Condé-Wolter, M.G. Ruf, A. Liebsch, T. Lebelt, I. Koch, K. Drechsler, M. Gude, Hydrogen permeability of thermoplastic composites and liner systems for future

mobility applications, Composites, Part A, Appl. Sci. Manuf. 167 (2023) 107446, https://doi.org/10.1016/j.compositesa.2023.107446.
[23] S. Schiessl, E. Kucukpinar, N. Rivollier, H.-C. Langowski, P. Eisner, A comparative study on the roll-to-roll processing of a silicate–polyvinyl alcohol composite barrier lacquer using slot-die and reverse gravure coating techniques, Polymers 15 (13) (2023), https://doi.org/10.3390/polym15132761.
[24] S. Matteucci, Y. Yampolskii, B.D. Freeman, I. Pinnau, Transport of Gases and Vapors in Glassy and Rubbery Polymers, John Wiley & Sons, Ltd, 2006, pp. 1–47, Ch. 1.
[25] L.E. Nielsen, Models for the permeability of filled polymer systems, J. Macromol. Sci., Part A, Chem. 1 (1967) 929–942, https://doi.org/10.1080/10601326708053745.
[26] DIN Deutsches Institut für Normung e.V., Paints and varnishes – wettability – part 3: determination of the surface tension of liquids using the pendant drop method (iso 19403-3:2017), DIN EN ISO 19403-3 (April 2020).
[27] D.K. Owens, R. Wendt, Estimation of the surface free energy of polymers, J. Appl. Polym. Sci. 13 (8) (1969) 1741–1747, https://doi.org/10.1002/app.1969.070130815.
[28] DIN Deutsches Institut für Normung e.V., Paints and varnishes – wettability – part 2: determination of the surface free energy of solid surfaces by measuring the contact angle (iso 19403-2:2017), DIN EN ISO 19403-2 (April 2020).
[29] M. Firon, S. Cros, P. Trouslard, Method and device for measurement of permeation, U.S. Patent US2007186622, 2007.
[30] R.M. Barrer, Diffusion in and Through Solids, University Press, 1941.
[31] DIN Deutsches Institut für Normung e.V., Determining the gas transmission rate of plastic film, sheeting and mouldings by the carrier gas method, DIN 53380-3 (June 1998).
[32] DIN Deutsches Institut für Normung e.V., Plastics - film and sheeting - determination of water vapour transmission rate, DIN EN ISO 15106-3 (May 2005).
[33] R.K. Bharadwaj, Modeling the barrier properties of polymer-layered silicate nanocomposites, Macromolecules 34 (26) (2001) 9189–9192, https://doi.org/10.1021/ma010780b.
[34] L. Shen, Z. Chen, Critical review of the impact of tortuosity on diffusion, Chem. Eng. Sci. 62 (2007) 3748–3755, https://doi.org/10.1016/j.ces.2007.03.041.
[35] B. Jańczuk, T. Białopiotrowicz, W. Wójcik, The components of surface tension of liquids and their usefulness in determinations of surface free energy of solids, J. Colloid Interface Sci. 127 (1) (1989) 59–66, https://doi.org/10.1016/0021-9797(89)90007-6.
[36] K. Norrish, The swelling of montmorillonite, Discuss. Faraday Soc. 18 (1954) 120–134, https://doi.org/10.1039/DF9541800120.
[37] A.M. Atta, H.A. Al-Lohedan, Z. Alothman, A.A. Abdel-Khalek, A.M. Tawfeek, Characterization of reactive amphiphilic montmorillonite nanogels and its application for removal of toxic cationic dye and heavy metals water pollutants, J. Ind. Eng. Chem. 31 (2015) 374–384, https://doi.org/10.1016/j.jiec.2015.07.012.
[38] V. Khoshkava, M.R. Kamal, Effect of surface energy on dispersion and mechanical properties of polymer/nanocrystalline cellulose nanocomposites, Biomacromolecules 14 (9) (2013) 3155–3163, https://doi.org/10.1021/bm400784j, pMID: 23927495.
[39] A. Habib, M. Abd-El-Megeed, A. Saafan, R. Issa, The catalytic conversion of n-pentanol to dialkylether by some cation-exchanged montmorillonite catalysts, J. Incl. Phenom. 4 (1986) 185–189, https://doi.org/10.1007/BF00655933.
[40] S. Abend, G. Lagaly, Sol–gel transitions of sodium montmorillonite dispersions, Appl. Clay Sci. 16 (3) (2000) 201–227, https://doi.org/10.1016/S0169-1317(99)00040-X.
[41] R.H. Ellerbrock, A. Höhn, J. Rogasik, Functional analysis of soil organic matter as affected by long-term manurial treatment, Eur. J. Soil Sci. 50 (1) (1999) 65–71, https://doi.org/10.1046/j.1365-2389.1999.00206.x.
[42] A.A. Tireli, I.d.R. Guimarães, J.C.d.S. Terra, R.R. da Silva, M.C. Guerreiro, Fenton-like processes and adsorption using iron oxide-pillared clay with magnetic properties for organic compound mitigation, Environ. Sci. Pollut. Res. 22 (2) (2015) 870–881, https://doi.org/10.1007/s11356-014-2973-x.
[43] V. Krylova, N. Dukštienė, Synthesis and characterization of Ag_2S layers formed on polypropylene, J. Chem. 2013 (2013) 987879, https://doi.org/10.1155/2013/987879.
[44] D. Xiao, D. Chen, Z. Zhou, A. Zhong, Three-group type mechanism in the curing behavior of polyacrylate and blocked toluene diisocyanate, J. Appl. Polym. Sci. 83 (2002) 112–120, https://doi.org/10.1002/app.2233.
[45] D. Liang, C. Du, F. Ma, Y. Shen, K. Wu, J. Zhou, Characterization of nano FeIII-tannic acid modified polyacrylate in controlled-release coated urea by Fourier transform infrared photoacoustic spectroscopy and laser-induced breakdown spectroscopy, Polym. Test. 64 (2017) 101–108, https://doi.org/10.1016/j.polymertesting.2017.09.037.
[46] A.S. Asran, S. Henning, G.H. Michler, Polyvinyl alcohol–collagen–hydroxyapatite biocomposite nanofibrous scaffold: mimicking the key features of natural bone at the nanoscale level, Polymer 51 (4) (2010) 868–876, https://doi.org/10.1016/j.polymer.2009.12.046.
[47] H. Qin, S. Zhang, C. Zhao, M. Feng, M. Yang, Z. Shu, S. Yang, Thermal stability and flammability of polypropylene/montmorillonite composites, Polym. Degrad. Stab. 85 (2) (2004) 807–813, https://doi.org/10.1016/j.polymdegradstab.2004.03.014.
[48] B. Albach, M. Munaro, P.H. Santos, S.F. Zawadzki, W.H. Schreiner, D.S. Rampon, R.V. Barbosa, Thermal, mechanical, and water vapor barrier behavior of polypropylene composite containing modified kaolinite, J. Appl. Polym. Sci. 135 (5) (2018) 45785, https://doi.org/10.1002/app.45785.
[49] N. Bunekar, T.-Y. Tsai, J.-Y. Huang, S.-J. Chen, Investigation of thermal, mechanical and gas barrier properties of polypropylene-modified clay nanocomposites by micro-compounding process, J. Taiwan Inst. Chem. Eng. 88 (2018) 252–260, https://doi.org/10.1016/j.jtice.2018.04.016.
[50] R. Ianchis, L. Cinteza, D. Donescu, C. Petcu, M. Corobea, R. Somoghi, M. Ghiurea, C. Spataru, Implications of silylated montmorillonite on montmorillonite–polyacrylate nanocomposites, Appl. Clay Sci. 52 (1) (2011) 96–103, https://doi.org/10.1016/j.clay.2011.02.004.
[51] B. Smith, Infrared spectroscopy of polymers X: polyacrylates, Spectroscopy 38 (01) (2023) 10–14, https://www.spectroscopyonline.com/view/infrared-spectroscopy-of-polymers-x-polyacrylates.
[52] M.-C. Lai, K.-C. Chang, J.-M. Yeh, S.-J. Liou, M.-F. Hsieh, H.-S. Chang, Advanced environmentally friendly anticorrosive materials prepared from water-based polyacrylate/Na+-MMT clay nanocomposite latexes, Eur. Polym. J. 43 (10) (2007) 4219–4228, https://doi.org/10.1016/j.eurpolymj.2007.05.008.
[53] P. Natkański, P. Kuśtrowski, A. Białas, Z. Piwowarska, M. Michalik, Controlled swelling and adsorption properties of polyacrylate/montmorillonite composites, Mater. Chem. Phys. 136 (2) (2012) 1109–1115, https://doi.org/10.1016/j.matchemphys.2012.08.061.
[54] C. Yu, R. Liao, X. Cai, X. Yu, Sodium polyacrylate modification method to improve the permeant performance of bentonite in chemical resistance, J. Clean. Prod. 213 (2019) 242–250, https://doi.org/10.1016/j.jclepro.2018.12.179.
[55] B. Behera, P.K. Das, Blue- and red-shifting hydrogen bonding: a gas phase FTIR and ab initio study of RR'CO· · ·DCCl3 and RR'S· · ·DCCl3 complexes, J. Phys. Chem. A 122 (18) (2018) 4481–4489, https://doi.org/10.1021/acs.jpca.7b11962, pMID: 29683668.
[56] A. Błoniarz, J. Marchewka, M. Sitarz, K. Drożdż, T. Gosiewski, M. Brzychczy-Włoch, T. Moskalewicz, Effect of adding selected carboxylic acids to the solution on electrophoretic deposition, adhesion strength, morphology and antibacterial properties of chitosan coatings on titanium, Prog. Org. Coat. 189 (2024) 108258, https://doi.org/10.1016/j.porgcoat.2024.108258.
[57] S. Spoljaric, A. Salminen, N. Dang Luong, P. Lahtinen, J. Vartiainen, T. Tammelin, J. Seppälä, Nanofibrillated cellulose, poly(vinyl alcohol), montmorillonite clay hybrid nanocomposites with superior barrier and thermomechanical properties, Polym. Compos. 35 (6) (2014) 1117–1131, https://doi.org/10.1002/pc.22759.
[58] M.A. Mballa Mballa, S.I. Ali, J.P. Heuts, A.M. van Herk, Control of the anisotropic morphology of latex nanocomposites containing single montmorillonite clay particles prepared by conventional and reversible addition-fragmentation chain transfer based emulsion polymerization, Polym. Int. 61 (6) (2012) 861–865, https://doi.org/10.1002/pi.4185.
[59] M.-J. Dumont, A. Reyna-Valencia, J.-P. Emond, M. Bousmina, Barrier properties of polypropylene/organoclay nanocomposites, J. Appl. Polym. Sci. 103 (1) (2007) 618–625, https://doi.org/10.1002/app.25253.
[60] J. Villaluenga, M. Khayet, M. López-Manchado, J. Valentin, B. Seoane, J. Mengual, Gas transport properties of polypropylene/clay composite membranes, Eur. Polym. J. 43 (4) (2007) 1132–1143, https://doi.org/10.1016/j.eurpolymj.2007.01.018.
[61] D. Hu, J. Chen, S. Sun, T. Liu, L. Zhao, Solubility and diffusivity of CO2 in isotactic polypropylene/nanomontmorillonite composites in melt and solid states, Ind. Eng. Chem. Res. 53 (7) (2014) 2673–2683, https://doi.org/10.1021/ie403580x.
[62] D.-S. Chen, G.-H. Hsiue, C.-S. Hsu, Gas permeation through two side-chain liquid-crystalline polyacrylate-based membranes containing 4-methoxyphenyl 4-hexyloxybenzoate or 4-cyanophenyl 4-hexyloxybenzoate mesogenic side groups, Makromol. Chem. 193 (6) (1992) 1469–1479, https://doi.org/10.1002/macp.1992.021930623.
[63] P. Tzeng, E.L. Lugo, G.D. Mai, B.A. Wilhite, J.C. Grunlan, Super hydrogen and helium barrier with polyelectolyte nanobrick wall thin film, Macromol. Rapid Commun. 36 (1) (2015) 96–101, https://doi.org/10.1002/marc.201400559.
[64] J.M. Herrera-Alonso, Z. Sedláková, E. Marand, Gas transport properties of polyacrylate/clay nanocomposites prepared via emulsion polymerization, J. Membr. Sci. 363 (1) (2010) 48–56, https://doi.org/10.1016/j.memsci.2010.07.014.
[65] J.C. Grunlan, A. Grigorian, C.B. Hamilton, A. Mehrabi, Effect of clay concentration on the oxygen permeability and optical properties of a modified poly(vinyl alcohol), J. Appl. Polym. Sci. 93 (2004) 1102–1109, https://doi.org/10.1002/app.20564.
[66] Y. Song, J. Gerringer, S. Qin, J.C. Grunlan, High oxygen barrier thin film from aqueous polymer/clay slurry, Ind. Eng. Chem. Res. 57 (2018) 6904–6909, https://doi.org/10.1021/acs.iecr.8b01077.
[67] S. Schiessl, P. Eisner, E. Kucukpinar, Gasbarriereschicht, Nanokomposit-Lack zur Erzeugung der Gasbarriereschicht sowie Verfahren zur Herstellung des Lacks, Patent WO23072628 A1, 2023.
[68] C. Habel, E.S. Tsurko, R.L. Timmins, J. Hutschreuther, R. Kunz, D.D. Schuchardt, S. Rosenfeldt, V. Altstädt, J. Breu, Lightweight ultra-high-barrier liners for helium and hydrogen, ACS Nano 14 (6) (2020) 7018–7024, https://doi.org/10.1021/acsnano.0c01633, pMID: 32374585.
[69] H. Kim, W. Choi, S.E. Choi, K. Nomura, J.-W. Kwark, C.J. Ellison, D.W. Kim, Tailored self-assembly of semi-transparent polymer/clay nanocomposites for gas-barrier applications assisted by aqueous liquid crystalline scaffolds, Prog. Org. Coat. 186 (2024) 108003, https://doi.org/10.1016/j.porgcoat.2023.108003.

[70] M.C. Celina, A. Quintana, Oxygen diffusivity and permeation through polymers at elevated temperature, Polymer 150 (2018) 326–342, https://doi.org/10.1016/j.polymer.2018.06.047.

[71] J. Kim, Y. Lin, Synthesis and oxygen permeation properties of ceramic-metal dual-phase membranes, J. Membr. Sci. 167 (1) (2000) 123–133, https://doi.org/10.1016/S0376-7388(99)00273-2.

[72] A.G. Erlat, B.-C. Wang, R.J. Spontak, Y. Tropsha, K.D. Mar, D.B. Montgomery, E.A. Vogler, Morphology and gas barrier properties of thin SiOxcoatings on polycarbonate: correlations with plasma-enhanced chemical vapor deposition conditions, J. Mater. Res. 15 (3) (2000) 704–717, https://doi.org/10.1557/JMR.2000.0103.

[73] K. Sankaran, P. Manoharan, S.R. S, S. Chattopadhyay, A brief insight into the prediction of water vapor transmissibility in highly impermeable hybrid nanocomposites based on bromobutyl/epichlorohydrin rubber blends, Open Chem. 16 (1) (2018) 1207–1213, https://doi.org/10.1515/chem-2018-0124.

[74] S. Kumar, S. Chattopadhyay, A. Sreejesh, S. Nair, G. Unnikrishnan, G.B. Nando, Analysis of air permeability and WVTR characteristics of highly impermeable novel rubber nanocomposite, Mater. Res. Express 2 (2) (2015) 025001, https://doi.org/10.1088/2053-1591/2/2/025001.

[75] J. Li, X. Li, K. Wu, D. Feng, T. Zhang, Y. Zhang, Thickness and stability of water film confined inside nanoslits and nanocapillaries of shale and clay, Int. J. Coal Geol. 179 (2017) 253–268, https://doi.org/10.1016/j.coal.2017.06.008.

[76] D. Murima, H. Pfukwa, I. Tiggelman, P.C. Hartmann, H. Pasch, Novel polymer clay-based nanocomposites: films with remarkable optical and water vapor barrier properties, Macromol. Mater. Eng. 301 (7) (2016) 836–845, https://doi.org/10.1002/mame.201600080.

[77] T.T.T. Ho, T. Zimmermann, S. Ohr, W.R. Caseri, Composites of cationic nanofibrillated cellulose and layered silicates: water vapor barrier and mechanical properties, ACS Appl. Mater. Interfaces 4 (9) (2012) 4832–4840, https://doi.org/10.1021/am3011737, pMID: 22928612.

[78] U.M. Garusinghe, S. Varanasi, V.S. Raghuwanshi, G. Garnier, W. Batchelor, Nanocellulose-montmorillonite composites of low water vapour permeability, Colloids Surf. A, Physicochem. Eng. Asp. 540 (2018) 233–241, https://doi.org/10.1016/j.colsurfa.2018.01.010.